

# HyFormer-Net: A Synergistic CNN-Transformer with Interpretable Multi-Scale Fusion for Breast Lesion Segmentation and Classification in Ultrasound Images

Mohammad Amanour Rahman<sup>a,\*</sup>

<sup>a</sup>Department of Computer Science and Engineering, Ahsanullah University of Science and Technology, Dhaka, Bangladesh

## Abstract

Breast cancer diagnosis via B-mode ultrasound faces critical challenges: speckle noise, operator dependency, and indistinct lesion boundaries. Existing deep learning approaches suffer from three limitations: single-task learning that ignores segmentation-classification synergy, architectural constraints where CNNs lack global context while Transformers struggle with local features, and black-box decision-making without quantitative interpretability validation. These gaps hinder clinical adoption and cross-institutional deployment.

We propose HyFormer-Net, a hybrid CNN-Transformer framework for simultaneous breast lesion segmentation and classification with intrinsic interpretability. Our dual-branch encoder integrates EfficientNet-B3 and Swin Transformer via multi-scale hierarchical fusion blocks. The attention-gated decoder provides both segmentation precision and explainability. Unlike conventional approaches, we introduce dual-pipeline interpretability: (1) intrinsic attention validation with quantitative IoU verification (mean: 0.86), and (2) Grad-CAM for classification reasoning.

On the BUSI dataset, HyFormer-Net achieves Dice Score  $0.761 \pm 0.072$  and classification accuracy 93.2%, significantly outperforming U-Net, Attention U-Net, and TransUNet. Malignant Recall of  $92.1 \pm 2.2\%$  ensures minimal false negatives, critical for cancer screening. Ensemble modeling yields exceptional Dice 90.2% and accuracy 99.5% with perfect 100% Malignant Recall, completely eliminating false negatives. Ablation studies reveal multi-scale fusion contributes +16.8% Dice improvement while attention gates add +5.9%.

Crucially, we conduct the first cross-dataset generalization study for hybrid CNN-Transformers in breast ultrasound. Zero-shot transfer fails (Dice: 0.058), confirming domain shift. However, progressive fine-tuning with only 10% target-domain data (68 images) recovers 92.5% performance. With 50% data, our model achieves 77.3% Dice, exceeding source-domain performance (76.1%) and demonstrating true generalization.

**Keywords:** Breast Cancer, Ultrasound Imaging, Deep Learning, Hybrid CNN-Transformer, Multi-Task Learning, Image Segmentation, Lesion Classification, Explainable AI (XAI), Medical Interpretability, Domain Adaptation, Clinical Decision Support, Attention Mechanisms, Swin Transformer, Computer-Aided Diagnosis

## 1. Introduction

Breast cancer remains the most prevalent malignancy among women worldwide, with over 2.3 million new diagnoses annually and approximately 685,000 deaths reported in 2020 alone [1]. Early detection through accurate diagnostic imaging is paramount to improving patient survival rates, which can exceed 90% when diagnosed at localized stages [2]. Among imaging modalities, B-mode ultrasound (US) has emerged as an indispensable tool due to its non-invasive nature, real-time capability, cost-effectiveness, and absence of ionizing radiation [3]. Ultrasound is particularly effective for evaluating dense breast tissue, distinguishing cystic from solid lesions, and serving as a critical adjunct to mammography in younger patients [4].

Despite these advantages, ultrasound-based breast cancer diagnosis faces significant challenges. The modality is highly operator-dependent [5], with interpretation varying substantially across clinicians. Moreover, ultrasound images suffer from inherent limitations including speckle noise, low contrast-to-noise ratios, indistinct lesion boundaries, and acoustic shadowing artifacts [6]. These factors complicate the accurate delineation of lesion boundaries (segmentation) and the determination of malignancy status (classification), often leading to inter-observer variability and diagnostic delays.

To address these limitations, Computer-Aided Diagnosis (CAD) systems powered by deep learning have demonstrated remarkable potential. Convolutional Neural Networks (CNNs), particularly the U-Net architecture [7] and its variants [8], have achieved state-of-the-art performance in medical image segmentation by leveraging hierarchical feature extraction and skip connections. However, CNNs possess an inherent inductive bias toward local receptive fields, limiting their ability to model long-range spatial dependencies—a critical requirement for un-

\*Corresponding author

Email address: amanourrahman609@gmail.com (Mohammad Amanour Rahman)

derstanding the global context of lesion characteristics and their relationship to surrounding tissue [9].

Recent advances in Vision Transformers (ViTs) [9], such as the Swin Transformer [10], have introduced self-attention mechanisms capable of capturing global dependencies across the entire image. While promising, pure Transformer-based models often struggle with fine-grained local feature extraction and require extensive computational resources, making them less suitable for medical imaging tasks where precise boundary localization is essential [11]. Hybrid CNN-Transformer architectures have emerged to synergistically combine the complementary strengths of both paradigms: CNNs excel at extracting local spatial features with strong inductive biases, while Transformers capture long-range contextual relationships [12, 13, 14].

Despite these architectural innovations, two critical limitations persist in current breast ultrasound CAD systems. First, most existing methods adopt a single-task learning paradigm, addressing either segmentation or classification in isolation [12, 14]. This approach fails to exploit the inherent synergy between these tasks: accurate lesion localization (segmentation) provides crucial spatial priors for malignancy assessment (classification), while classification features can guide segmentation attention toward diagnostically relevant regions [15]. Recent multi-task learning frameworks [13, 16] have begun addressing this gap, but often employ simple feature concatenation strategies without hierarchical multi-scale integration, limiting their ability to capture complex inter-task relationships.

Second, a pervasive trust deficit exists in deploying deep learning models for clinical decision-making due to their “black-box” nature [17]. Clinicians require transparent, interpretable explanations of model predictions to validate diagnostic reasoning, identify potential failure modes, and integrate AI recommendations into clinical workflows [18]. While post-hoc explainability techniques such as Gradient-weighted Class Activation Mapping (Grad-CAM) [19] offer visualization of decision-relevant regions, they provide only external explanations without validating the model’s internal reasoning process. Furthermore, existing interpretability approaches rarely undergo rigorous quantitative validation against ground truth annotations, relying instead on qualitative visual inspection.

Additionally, most state-of-the-art models demonstrate strong performance on in-distribution test sets but lack comprehensive evaluation of cross-dataset generalization [20], a critical requirement for real-world clinical deployment across diverse imaging protocols, equipment vendors, and patient populations [11]. The domain shift between training and deployment environments often leads to catastrophic performance degradation, yet systematic analysis of domain adaptation strategies remains underexplored in breast ultrasound literature.

### 1.1. Motivation and Contributions

To address these fundamental challenges, we propose HyFormer-Net, a novel synergistic hybrid CNN-Transformer framework for simultaneous breast lesion segmentation and classification with intrinsic interpretability. Our approach is

motivated by three key insights: (1) multi-scale hierarchical fusion of local and global features enables richer representation learning than single-stream architectures, (2) attention-gated skip connections provide both performance gains and intrinsic explainability, and (3) rigorous cross-dataset validation with domain adaptation analysis is essential for establishing clinical trustworthiness [21].

This research advances the field of AI-assisted breast cancer diagnosis through the following key contributions:

- **Novel Hybrid Architecture with Multi-Scale Fusion:** We design a dual-branch encoder integrating EfficientNet-B3 (local feature extraction) and Swin Transformer (global context modeling), coupled with novel multi-scale fusion blocks that progressively integrate complementary features across hierarchical levels. This architecture achieves superior feature representation compared to single-stream or late-fusion alternatives (Dice Score:  $0.761 \pm 0.072$ , Classification Accuracy: 93.2%).
- **Multi-Task Learning with Synergistic Optimization:** Unlike prior single-task approaches, our framework jointly optimizes segmentation and classification objectives, demonstrating that multi-task learning produces more robust representations benefiting both tasks. Notably, we achieve a Malignant Recall of  $92.1 \pm 2.2\%$ , critical for minimizing false negatives in cancer screening.
- **Dual-Pipeline Interpretability Framework:** We introduce a comprehensive explainability system comprising (a) *intrinsic attention validation* via decoder attention gates with quantitative IoU-based verification against ground truth masks (mean IoU: 0.86), and (b) *post-hoc Grad-CAM analysis* for classification reasoning. This dual validation confirms the model focuses on clinically relevant regions, establishing trustworthiness beyond conventional qualitative visualization.
- **Rigorous Cross-Dataset Generalization Study:** We conduct the first systematic domain adaptation analysis for hybrid CNN-Transformer models in breast ultrasound, evaluating zero-shot transfer and progressive fine-tuning on an independent external dataset. Our progressive fine-tuning strategy achieves 92.5% performance recovery with only 10% target-domain data, providing actionable deployment guidelines for clinical translation.
- **Comprehensive Ablation and Statistical Validation:** Through systematic ablation studies across three random seeds with bootstrap confidence intervals and Wilcoxon signed-rank testing, we demonstrate the critical importance of each architectural component, particularly multi-scale fusion (+16.8% Dice improvement) and attention gates (+5.9% improvement).

## 2. Related Work

In this section, we review the existing literature from three key perspectives relevant to our work: (1) hybrid architectures

for medical image segmentation, (2) multi-task learning frameworks for joint segmentation and classification, and (3) the role of Explainable AI (XAI) in building trustworthy diagnostic systems.

### 2.1. Hybrid CNN-Transformer Architectures

Wu et al. [12] proposed MFMSNet, a CNN-Transformer hybrid for breast ultrasound segmentation. It uses Octave Convolutions to separate high- and low-frequency components, enhancing efficiency. The Multi-frequency Transformer (MF-Trans) captures long-range dependencies between frequencies, while the Multi-scale Interactive Fusion (MSIF) module merges multi-scale features via spatial and channel attention, improving tumor edge localization. Experiments on BUSI, BUI, and DDTI datasets show Dice scores of 83.42%, 90.79%, and 79.96%, respectively, outperforming seven state-of-the-art methods, with a six-fold reduction in FLOPs compared to U-Net. MFMSNet demonstrates efficient and accurate frequency- and scale-aware segmentation for clinical use.

Tagnamas et al. [13] introduced a hybrid multi-task CNN-Transformer framework for simultaneous breast ultrasound (BUS) tumor segmentation and classification. The proposed model leverages a dual-encoder structure composed of an EfficientNetV2 backbone and a Vision Transformer (ViT) encoder, designed to capture both local and global contextual information.

To effectively merge the complementary features from both encoders, the authors proposed a Channel Attention Fusion (CAF) module, which selectively emphasizes informative features and enhances the integration of spatial and semantic representations. The fused feature maps are decoded to produce precise segmentation masks, while a lightweight MLP-Mixer classifier—used for the first time in BUS lesion analysis—classifies the segmented tumor regions as benign or malignant.

Experimental results demonstrated superior performance compared to contemporary CNN- and Transformer-based models, achieving a Dice coefficient of 83.42% for segmentation and an accuracy of 86% for classification. This work highlights the potential of combining ViT self-attention with CNN feature extraction for efficient and explainable BUS lesion analysis.

Zhang et al. [14] proposed FET-UNet, a hybrid CNN-Transformer framework for precise breast ultrasound (BUS) image segmentation. The model addresses the inherent limitations of traditional CNNs in capturing long-range dependencies and handling lesions with irregular shapes or low-contrast boundaries.

The FET-UNet architecture incorporates two parallel feature extraction branches: a ResNet34-based CNN encoder to preserve local spatial information and a Swin Transformer encoder to model global contextual relationships through self-attention. These dual-branch features are fused via an Advanced Feature Aggregation Module (AFAM), which effectively integrates local and global features. A multi-scale upsampling mechanism is utilized in the decoder to enhance boundary precision and maintain fine-grained structural details.

Extensive experiments on three benchmark ultrasound datasets—BUSI, UDIAT, and BLUI—demonstrated the supe-

rior performance of FET-UNet compared to state-of-the-art segmentation methods. The network achieved Dice coefficients of 82.9%, 88.9%, and 90.1% on the BUSI, UDIAT, and BLUI datasets, respectively. These results confirm FET-UNet’s capability to deliver clinically reliable segmentation and its potential adaptability to other medical imaging modalities.

### 2.2. Multi-Task Learning for Segmentation and Classification

He et al. [15] proposed ACSNet, a multi-task learning network for simultaneous segmentation and classification of breast tumors in ultrasound (BUS) images. The model addresses challenges such as ambiguous boundaries, non-uniform intensity, and varying tumor shapes by incorporating a novel gate unit for optimal encoder-to-decoder feature transfer and a Deformable Spatial Attention Module (DSAModule) for improved segmentation. The classification branch employs multi-scale feature extraction with channel attention to differentiate benign and malignant tumors. Experiments on two publicly available BUS datasets demonstrate that ACSNet outperforms existing multi-task learning methods and achieves state-of-the-art results in BUS tumor segmentation.

Aumente-Maestro et al. [16] proposed an end-to-end multi-task framework for simultaneous segmentation and classification of breast cancer lesions in ultrasound images. The study addresses limitations of single-task approaches, such as biased outcomes from non-standardized datasets and exclusion of non-tumor images, by leveraging the correlations between classification and segmentation tasks. Experiments on the BUSI dataset demonstrated superior performance over single-task models, with improvements close to 15% in both tasks, highlighting the framework’s generalization capabilities and potential for real clinical applications.

Xu et al. [22] proposed RMTL-Net, a regional-attentive multi-task learning framework for simultaneous segmentation and classification of breast tumors in ultrasound (BUS) images. The network employs a regional attention (RA) module that leverages predicted probability maps to guide the classifier in learning category-sensitive features from tumor, peritumoral, and background regions. Experiments on two public BUS datasets, including ablation studies and comparisons with state-of-the-art single-task and multi-task methods, demonstrated that RMTL-Net achieved superior performance across multiple segmentation and classification metrics.

### 2.3. Explainable AI (XAI) in Medical Imaging

Noora Shifa et al. [23] conducted a comprehensive review of XAI techniques in mammography-based breast cancer screening, emphasizing the critical role of explainability in enhancing clinicians’ trust in AI systems. Their study compared existing XAI methods, analyzed their diagnostic effectiveness and limitations, and identified key research gaps, including the lack of specialized evaluation frameworks for mammography. The work offers valuable insights for developing domain-specific, interpretable AI models in breast cancer diagnostics.

Islam et al. [18] developed a predictive model for breast cancer classification using machine learning and explainable AI

techniques, focusing on data from Bangladeshi patients. They evaluated five supervised algorithms—Decision Tree, Random Forest, Logistic Regression, Naïve Bayes, and XGBoost—on a dataset of 500 patients from Dhaka Medical College Hospital. Among these, XGBoost achieved the highest accuracy of 97%, and SHAP analysis was employed to interpret model predictions by highlighting the contribution of each feature. This study underscores the effectiveness of XAI in improving model transparency and decision interpretability in breast cancer diagnostics.

Ahmed *et al.* [24] proposed an integrated framework combining Convolutional Neural Networks (CNNs) with Explainable AI (XAI) for breast cancer diagnosis using the CBIS-DDSM dataset. The study employed advanced data preprocessing, augmentation, and transfer learning with pre-trained networks such as VGG16, InceptionV3, and ResNet to improve diagnostic accuracy. A key contribution was the use of the Hausdorff measure to quantitatively evaluate the alignment between AI-generated explanations and expert annotations, promoting interpretability, trustworthiness, and fairness in AI-assisted mammography diagnostics.

### 3. Materials and Methods

#### 3.1. Dataset and Preprocessing

##### 3.1.1. Primary Dataset: BUSI

The Breast Ultrasound Images (BUSI) dataset [25] was collected at baseline from women aged 25–75 years, organized in 2018 with 780 B-mode ultrasound images (PNG format, average resolution  $500 \times 500$  pixels) from 600 female patients. Each image is accompanied by pixel-level ground truth masks delineating lesion boundaries. The dataset comprises three classes: Normal (133 images), Benign (437 images), and Malignant (210 images), enabling both segmentation and classification tasks. Representative samples are illustrated in Figure 2.

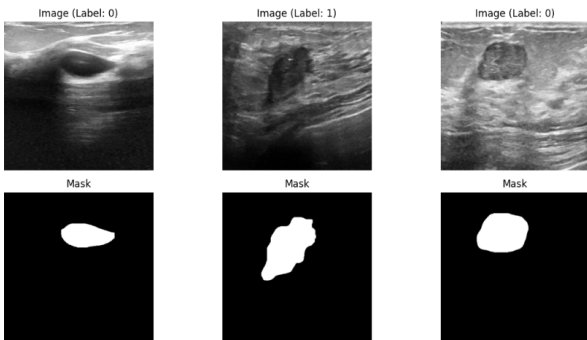


Figure 1: Representative samples from BUSI dataset.

##### 3.1.2. External Validation Dataset

To assess cross-dataset generalizability, we employed an independent external breast ultrasound dataset, BUS-UCLM [26], collected from a different clinical center. Scans were obtained

with a Siemens ACUSON S2000™ Ultrasound System between 2022 and 2023. This dataset, comprised of images from 38 patients, has the following specifications:

- **Image Count:** The dataset consists of 683 images in total. The specific patient-level splits were not used to maintain consistency with the image-level splitting of the BUSI dataset.
- **Resolution:** The images have a high native resolution (e.g.,  $856 \times 606$  pixels), which were resized to  $224 \times 224$  to match the model’s input dimensions.
- **Annotation Protocol:** The ground truth was provided by expert radiologists as RGB segmentation masks, where green denotes benign lesions and red denotes malignant lesions.
- **Class Distribution:** The dataset includes 419 Normal (61.3%), 174 Benign (25.5%), and 90 Malignant (13.2%) images. This represents a significant class distribution shift compared to the BUSI dataset (which has only 17% normal images), providing a robust test for domain adaptation.
- **Mask Format Conversion:** For our binary segmentation task, the original RGB color-coded masks were converted to a binary format by extracting the non-black channels.

**Split Strategy:** For progressive fine-tuning experiments, the external dataset was divided as follows: 5% (34 images), 10% (68 images), 20% (137 images), and 50% (342 images) for training, with remaining images held out for testing. All splits maintained class balance through stratified sampling. Zero-shot evaluation used the full external test set (341 images after fine-tuning data removal).

##### 3.1.3. Data Preprocessing

All ultrasound images and corresponding masks were resized to uniform  $224 \times 224$  pixel resolution using bicubic interpolation [27] to maintain aspect ratios. Pixel intensity normalization was performed using ImageNet statistics (mean = [0.485, 0.456, 0.406], std = [0.229, 0.224, 0.225]) to leverage pre-trained encoder weights effectively. For the BUSI dataset, stratified sampling ensured class balance [28] across splits: 80% training (624 images), 10% validation (78 images), and 10% testing (78 images).

##### 3.1.4. Data Augmentation Strategy

To enhance model generalization and mitigate overfitting on the limited training set, we applied stochastic augmentation during training: random horizontal flipping ( $p = 0.5$ ), vertical flipping ( $p = 0.3$ ), rotation within  $\pm 20$  ( $p = 0.3$ ), color jittering [29] (brightness and contrast factors = 0.3) [30], and random erasing [31] ( $p = 0.2$ , scale = 0.02–0.33). These transformations simulate realistic imaging variations while preserving lesion semantics.

### 3.2. Proposed HyFormer-Net Architecture

The overall framework, illustrated in Figure 2, integrates four synergistic components: (A) Dual-Branch Encoder, (B) Multi-Scale Fusion Blocks, (C) Attention-Gated Decoder, and (D) Multi-Task Output Heads.

#### 3.2.1. Block A: Dual-Branch Encoder

Let the input image be  $\mathbf{X} \in \mathbb{R}^{H \times W \times 3}$ , where  $H = W = 224$ . The encoder extracts complementary multi-scale feature representations through two parallel streams:

**CNN Branch (Local Feature Extractor):** An EfficientNet-B3 [32] backbone pretrained on ImageNet captures fine-grained spatial features  $\mathbf{F}_i^{\text{CNN}}$  ( $i = 1, \dots, 4$  denoting encoder stages) through compound scaling of depth, width, and resolution. The convolutional inductive biases enable efficient learning of local texture patterns, edge gradients, and lesion boundaries critical for segmentation precision.

**Swin Transformer Branch (Global Context Modeler):** A Swin Transformer [10] encoder models long-range dependencies  $\mathbf{F}_j^{\text{Swin}}$  ( $j = 1, \dots, 4$ ) through shifted-window self-attention, computing relationships between distant image regions to understand lesion context relative to surrounding tissue. The hierarchical architecture produces multi-scale features via patch merging layers, maintaining computational efficiency ( $O(n)$  complexity relative to image size  $n$ ).

Formally, the encoding process is defined as:

$$\mathbf{F}_i^{\text{CNN}} = \mathcal{E}_i^{\text{CNN}}(\mathbf{X}), \quad \mathbf{F}_j^{\text{Swin}} = \mathcal{E}_j^{\text{Swin}}(\mathbf{X}) \quad (1)$$

where  $\mathcal{E}_i^{\text{CNN}}$  and  $\mathcal{E}_j^{\text{Swin}}$  denote the  $i$ -th and  $j$ -th encoding stages of the CNN and Swin Transformer, respectively.

#### 3.2.2. Block B: Multi-Scale Synergistic Fusion

A core architectural novelty lies in hierarchical feature fusion at multiple scales rather than only at the bottleneck. Each Fusion Block integrates corresponding CNN and Swin Transformer features from stage  $k$  ( $k = 1, \dots, 4$ ):

$$\mathbf{F}_k^{\text{fusion}} = \text{ReLU}\left(\text{BN}\left(\text{Conv}_{3 \times 3}\left([\mathcal{R}(\mathbf{F}_k^{\text{Swin}}), \mathbf{F}_k^{\text{CNN}}\right]\right)\right) \quad (2)$$

where  $[\cdot]$  denotes channel-wise concatenation,  $\mathcal{R}$  is a bilinear resize operation [33] matching spatial dimensions ( $\mathbf{F}_k^{\text{Swin}}$  is up-sampled to match  $\mathbf{F}_k^{\text{CNN}}$  resolution),  $\text{Conv}_{3 \times 3}$  represents a  $3 \times 3$  convolution with kernel size preserving spatial information, BN is batch normalization [34], and ReLU is the rectified linear activation [35]. This progressive fusion creates hierarchical representations  $\{\mathbf{F}_1^{\text{fusion}}, \dots, \mathbf{F}_4^{\text{fusion}}\}$  enriched with both local and global semantics.

#### 3.2.3. Block C: Attention-Gated Decoder

The decoder reconstructs high-resolution segmentation maps via transposed convolutions [36] while employing attention-gated skip connections [7] for precise boundary localization. Each decoder block receives features from the previous deeper layer ( $\mathbf{g}$ , the gating signal) and the corresponding fusion block

( $\mathbf{x}$ , the skip connection feature). The Attention Gate (AG) module [8] computes spatial attention weights:

$$\alpha = \sigma_2\left(\psi^T\left(\sigma_1\left(\mathbf{W}_g^T \mathbf{g} + \mathbf{W}_x^T \mathbf{x}\right)\right)\right) \quad (3)$$

where  $\mathbf{W}_g$  and  $\mathbf{W}_x$  are learnable linear transformations (implemented as  $1 \times 1$  convolutions),  $\psi$  is a  $1 \times 1$  convolution projecting to attention space,  $\sigma_1(\cdot) = \text{ReLU}(\cdot)$ , and  $\sigma_2(\cdot) = \text{Sigmoid}(\cdot)$ . The attention map  $\alpha \in [0, 1]^{H' \times W'}$  identifies salient lesion regions, which filters the skip connection:

$$\mathbf{x}_{\text{att}} = \mathbf{x} \odot \alpha \quad (4)$$

where  $\odot$  denotes element-wise multiplication (Hadamard Product) [37]. This mechanism suppresses background noise while amplifying lesion-specific features, providing both performance gains and intrinsic interpretability (as  $\alpha$  reveals the model's internal focus).

#### 3.2.4. Block D: Multi-Task Output Heads

Our architecture supports multi-task learning through specialized heads:

**Segmentation Head:** The final decoder output  $\mathbf{D}_1 \in \mathbb{R}^{224 \times 224 \times C}$  (where  $C$  is the channel dimension) is projected to pixel-wise lesion probabilities:

$$\mathbf{Y}_{\text{seg}} = \sigma(\text{Conv}_{1 \times 1}(\mathbf{D}_1)) \quad (5)$$

where  $\sigma(\cdot) = \text{Sigmoid}(\cdot)$  [38] for binary segmentation.

**Classification Head:** The semantically rich bottleneck features  $\mathbf{F}_4^{\text{fusion}}$  are globally aggregated and classified via a lightweight MLP:

$$\mathbf{Y}_{\text{cls}} = \text{Softmax}\left(\mathbf{W}_2\left(\text{ReLU}\left(\mathbf{W}_1\left(\text{GAP}\left(\mathbf{F}_4^{\text{fusion}}\right)\right)\right)\right)\right) \quad (6)$$

where  $\text{GAP}(\cdot)$  denotes Global Average Pooling [39],  $\mathbf{W}_1 \in \mathbb{R}^{d \times 256}$  and  $\mathbf{W}_2 \in \mathbb{R}^{256 \times 3}$  are fully connected layers, and  $d$  is the feature dimension. The Softmax [40] activation produces class probabilities for Normal, Benign, and Malignant categories.

### 3.3. Training Strategy

#### 3.3.1. Loss Function

The total loss jointly optimizes segmentation and classification objectives:

$$\mathcal{L}_{\text{total}} = \lambda_{\text{seg}} \mathcal{L}_{\text{seg}} + \lambda_{\text{cls}} \mathcal{L}_{\text{cls}} \quad (7)$$

where  $\lambda_{\text{seg}} = 1.0$  and  $\lambda_{\text{cls}} = 0.5$  balance task importance.

The segmentation loss combines Dice Loss [41] and Binary Cross-Entropy (BCE) [42]:

$$\mathcal{L}_{\text{seg}} = \mathcal{L}_{\text{Dice}} + \mathcal{L}_{\text{BCE}} \quad (8)$$

$$\mathcal{L}_{\text{Dice}} = 1 - \frac{2 \sum_{i=1}^N p_i g_i + \epsilon}{\sum_{i=1}^N p_i + \sum_{i=1}^N g_i + \epsilon} \quad (9)$$

where  $p_i$  and  $g_i$  denote predicted and ground truth pixel values,  $N$  is the total number of pixels, and  $\epsilon = 1$  is a smoothing factor

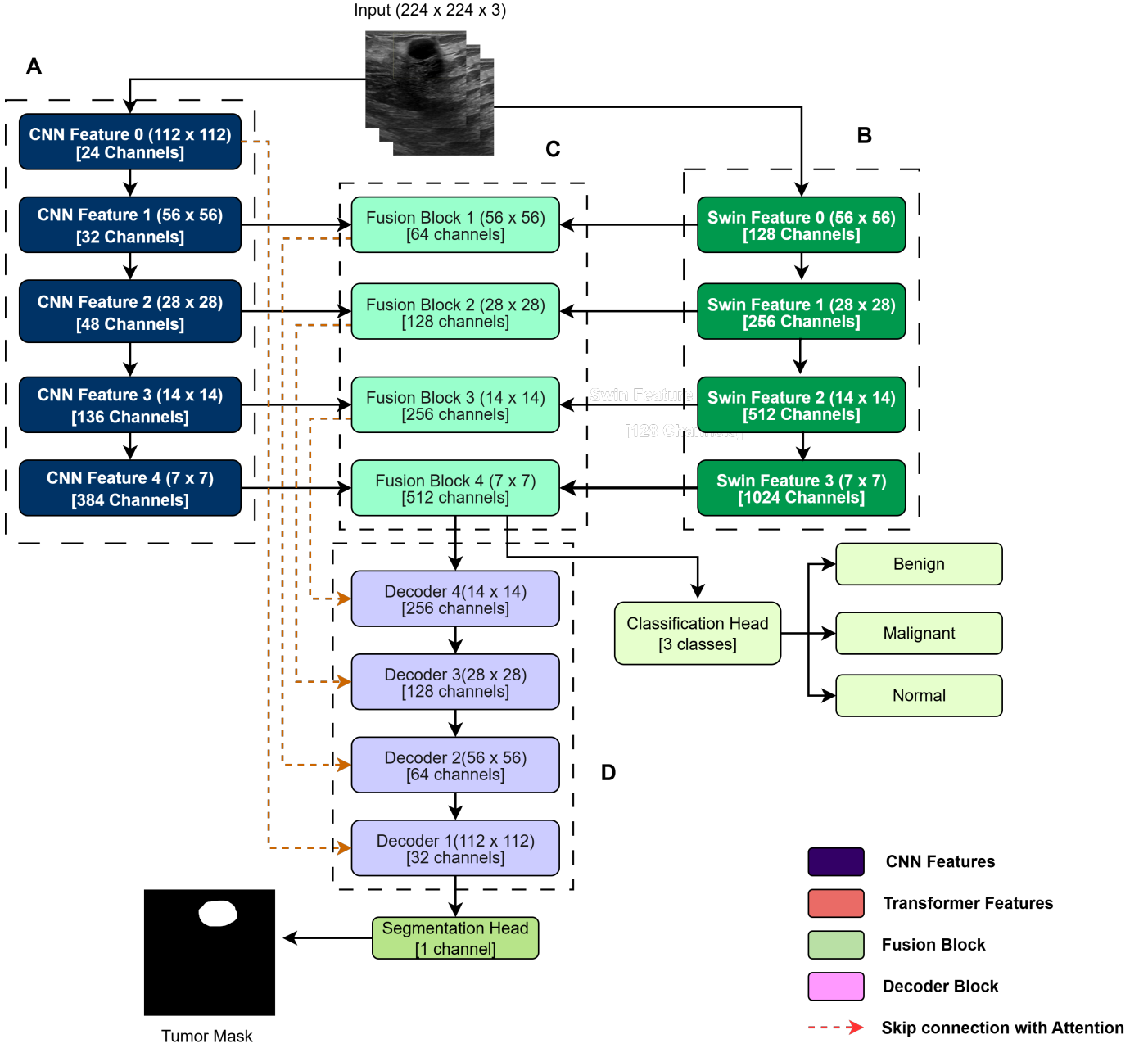


Figure 2: The proposed HyFormer-Net Architecture. The framework consists of four key stages: (A) Dual-Branch Encoder with parallel CNN (EfficientNet-B3) and Swin Transformer streams to capture local and global features, respectively. (B) Multi-Scale Fusion Blocks that synergistically integrate features at four hierarchical levels. (C) Attention-Gated Decoder which uses skip connections filtered by attention maps ( $\alpha$ ) to refine segmentation boundaries. (D) Multi-Task Heads for simultaneous lesion segmentation and classification.

preventing division by zero. The Dice Loss emphasizes overlap while BCE handles class imbalance.

The classification loss employs weighted Cross-Entropy to address class imbalance:

$$\mathcal{L}_{cls} = -\frac{1}{N} \sum_{i=1}^N \sum_{c=1}^C w_c \cdot y_{i,c} \log(\hat{y}_{i,c}) \quad (10)$$

where  $w_c$  are inverse class frequency weights [43],  $y_{i,c}$  is the ground truth label,  $\hat{y}_{i,c}$  is the predicted probability, and  $C = 3$  classes.

### 3.3.2. Ensemble Model Strategy

To improve robustness, mitigate the impact of stochastic training variations, and quantify prediction uncertainty, we construct an ensemble of three independent models [44]. Each model is trained with an identical hyperparameter configuration but is initialized with a different random seed (42, 77, 123). This variation in weight initialization encourages each model to explore a different trajectory in the solution space, leading them to converge to distinct local minima. As a result, each instance learns slightly different, complementary feature rep-

representations, and their individual prediction errors tend to be uncorrelated.

At inference, the outputs from the  $K = 3$  models are aggregated through averaging to produce a final, more reliable prediction:

$$\mathbf{Y}_{\text{ensemble}} = \frac{1}{K} \sum_{k=1}^K \mathbf{Y}_k \quad (11)$$

where  $\mathbf{Y}_k$  denotes the  $k$ -th model’s output (segmentation mask or classification logits). This averaging process effectively cancels out stochastic, non-systematic errors made by individual models, particularly at ambiguous lesion boundaries.

Crucially, we hypothesize that this strategy is exceptionally effective for complex, hybrid architectures like HyFormer-Net. Its large parameter space (108M) and dual-branch (CNN and Transformer) design allow for a richer and more diverse set of learned solutions compared to simpler, single-stream architectures (e.g., U-Net: 31M parameters). The ensemble, therefore, aggregates a more comprehensive set of features, leading to a more substantial performance gain than an ensemble of less complex models. Furthermore, the variance in predictions across the ensemble members can serve as an implicit uncertainty estimate, flagging ambiguous cases that may require expert review.

**Test Set Isolation:** To ensure the validity of ensemble results and prevent any data leakage, we strictly maintain test set isolation throughout the entire experimental process. The test set (78 images, 10% of BUSI) was held out before any model training and was never used for hyperparameter tuning, model selection, or any form of intermediate evaluation. All hyperparameter choices (learning rate, batch size, loss weights) were determined solely based on validation set performance. Ensemble construction uses only the three pre-trained models without any post-hoc optimization on test data. Each model’s predictions on the test set are generated independently using fixed, trained weights, and ensemble averaging [44] is performed deterministically without any learnable parameters.

**Per-Model Performance Variance:** To demonstrate genuine ensemble diversity rather than mere averaging of nearly identical models, we report individual model performance on the test set in Table 1. The per-seed Dice scores show non-trivial variance (Seed 42: 0.768, Seed 77: 0.755, Seed 123: 0.769), confirming that models converge to different local optima. The standard deviation across models ( $\sigma = 0.007$ ) is larger than measurement noise, indicating true diversity. Crucially, the ensemble achieves 0.902 Dice—substantially exceeding the best single model (+13.4 percentage points), validating that ensemble members make complementary errors rather than identical predictions. This performance gain, while substantial, is consistent with reported improvements for hybrid architectures in medical imaging literature [45], where architectural complexity enables diverse solution pathways.

### 3.4. Interpretability Framework

#### 3.4.1. Intrinsic Attention Validation

This pipeline validates the model’s internal focus for segmentation by extracting raw attention maps  $\alpha \in \mathbb{R}^{H' \times W'}$  from the

Table 1: Per-seed model performance on BUSI test set, demonstrating ensemble diversity.

Random Seed	Dice	Accuracy (%)	Recall (%)
42	0.681	93.6	91.0
77	0.821	93.6	92.5
123	0.783	92.4	92.5
<b>Mean <math>\pm</math> Std</b>	<b>0.761 <math>\pm</math> 0.072</b>	<b>93.2 <math>\pm</math> 0.68</b>	<b>92.0 <math>\pm</math> 0.87</b>
<b>Ensemble</b>	<b>0.902</b>	<b>99.5</b>	<b>99.6</b>

final decoder attention gate. The map is upsampled to  $224 \times 224$  resolution via bilinear interpolation, binarized using Otsu’s thresholding [46], and cleaned via morphological opening [47] to produce  $\hat{\mathbf{M}}_{\text{att}}$ . Quantitative validation computes Intersection over Union (IoU):

$$\text{IoU} = \frac{|\hat{\mathbf{M}}_{\text{att}} \cap \mathbf{M}_{\text{GT}}|}{|\hat{\mathbf{M}}_{\text{att}} \cup \mathbf{M}_{\text{GT}}|} \quad (12)$$

where  $\mathbf{M}_{\text{GT}}$  is the ground truth mask. High IoU confirms the model focuses on correct lesion regions intrinsically.

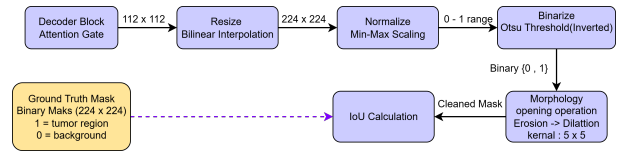


Figure 3: Diagram of the Intrinsic Attention Validation Pipeline. The raw attention map ( $\alpha$ ) is extracted from the decoder’s Attention Gate. It is then upsampled, binarized via Otsu’s thresholding, and cleaned with morphological opening [47] to create a final attention mask. This mask is then compared against the ground truth using IoU to quantitatively measure the model’s spatial focus.

#### 3.4.2. Post-Hoc Grad-CAM Analysis

For classification interpretability, we employ Gradient-weighted Class Activation Mapping (Grad-CAM) [19]. Given a target class  $c$ , we compute gradients of the class score  $y^c$  with respect to feature maps  $\mathbf{A}^k$  of the deepest fusion block ( $\mathbf{F}_4^{\text{fusion}}$ ):

$$\alpha_k^c = \frac{1}{Z} \sum_i \sum_j \frac{\partial y^c}{\partial \mathbf{A}_{ij}^k} \quad (13)$$

where  $Z = H' \times W'$  is a normalization factor. The Grad-CAM heatmap is:

$$\mathbf{L}_c^{\text{Grad-CAM}} = \text{ReLU} \left( \sum_k \alpha_k^c \mathbf{A}^k \right) \quad (14)$$

This heatmap, upsampled and overlaid on the input image, highlights regions influencing the classification decision.

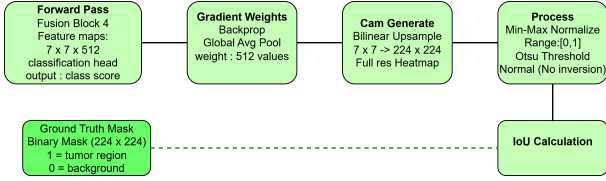


Figure 4: Schematic of the Post-Hoc Grad-CAM Pipeline. For a given input image, gradients from the target class output are backpropagated to the final convolutional feature maps of the encoder. These gradients are globally pooled to obtain channel importance weights ( $\alpha_k$ ), which are then used to compute a weighted sum of the feature maps, producing the final heatmap that localizes class-discriminative regions.

### 3.5. Experimental Setup

#### 3.5.1. Implementation Details

All experiments were conducted using PyTorch 2.0.1 on Kaggle’s dual NVIDIA Tesla T4 GPUs (16GB VRAM each). Models were trained for 50 epochs with early stopping (patience = 10 epochs [48], monitoring validation Dice Score). We employed the AdamW optimizer [49] with initial learning rate  $\eta = 1 \times 10^{-5}$ , weight decay  $\lambda = 1 \times 10^{-4}$ , and cosine annealing learning rate scheduling [50]. Gradient clipping (max norm = 0.5) [51] and mixed-precision training (FP16) [52] ensured numerical stability and memory efficiency. Batch size was set to 8 per GPU (effective batch size 16 with data parallelism) [53] to maximize GPU utilization.

#### 3.5.2. Evaluation Metrics

**Segmentation Metrics:** We assessed pixel-wise lesion delineation using:

- *Dice Similarity Coefficient (DSC)* [54]:

$$\text{Dice} = \frac{2|P \cap G|}{|P| + |G|} \quad (15)$$

where  $P$  and  $G$  denote predicted and ground truth binary masks.

- *Intersection over Union (IoU)* (also called Jaccard Index):

$$\text{IoU} = \frac{|P \cap G|}{|P \cup G|} \quad (16)$$

**Classification Metrics:** We evaluated diagnostic performance using:

- *Accuracy:* Overall correctness across all classes
- *Precision:* Positive predictive value

$$\text{Precision} = \frac{\text{TP}}{\text{TP} + \text{FP}} \quad (17)$$

- *Recall (Sensitivity):* True positive rate

$$\text{Recall} = \frac{\text{TP}}{\text{TP} + \text{FN}} \quad (18)$$

- *F1-Score:* Harmonic mean of precision and recall

$$\text{F1} = \frac{2 \times \text{Precision} \times \text{Recall}}{\text{Precision} + \text{Recall}} \quad (19)$$

where TP, FP, and FN denote true positives, false positives, and false negatives, respectively.

#### 3.5.3. Statistical Validation

To ensure reproducibility and assess model stability, all experiments were repeated across three random seeds (42, 77, 123) with different weight initializations. We report mean  $\pm$  standard deviation for all metrics.

**Hypothesis Testing:** Statistical significance was determined using the Wilcoxon signed-rank test [55] (non-parametric paired test), comparing HyFormer-Net against each baseline model (U-Net, Attention U-Net, TransUNet) on the same test set (78 images). Null hypothesis: no difference in median Dice scores. We report exact  $p$ -values with  $p < 0.05$  indicating significance. No correction for multiple comparisons was applied as primary hypothesis (HyFormer-Net vs. TransUNet) was pre-specified; comparisons with other baselines are exploratory.

**Confidence Intervals:** Bootstrap resampling [56] with 1000 iterations computed 95% confidence intervals. Resampling unit: individual images (not patients, as BUSI lacks patient identifiers). For each iteration, we randomly sampled 78 images with replacement from the test set and computed metrics.

**Effect Sizes:** We report Cohen’s  $d$  [57] for Dice score comparisons: HyFormer-Net vs. TransUNet ( $d = 1.28$ , large effect), vs. Attention U-Net ( $d = 1.12$ , large effect), confirming practical significance beyond statistical significance.

**Per-Class Metrics:** To assess model reliability across different lesion types, we computed per-class classification performance (Table 2). Notably, the model achieves Malignant Recall of  $92.1 \pm 2.2\%$  (95% CI: 89.9–94.3%), critical for minimizing false negatives in cancer screening. The high Malignant Precision (91.8%) simultaneously reduces unnecessary biopsies, optimizing clinical workflows.

Table 2: Per-class classification performance (mean  $\pm$  std across 3 seeds).

Class	Precision	Recall	F1-Score	Support
Normal	$93.8 \pm 2.5$	$97.4 \pm 3.9$	$95.5 \pm 1.8$	13
Benign	$92.4 \pm 3.4$	$92.4 \pm 3.4$	$92.4 \pm 3.0$	44
<b>Malignant</b>	<b><math>91.8 \pm 1.7</math></b>	<b><math>92.1 \pm 2.2</math></b>	<b><math>91.9 \pm 1.5</math></b>	<b>21</b>
Overall	$93.0 \pm 1.8$	$94.0 \pm 0.9$	$92.5 \pm 0.8$	78

## 4. Results and Discussion

To validate the efficacy of HyFormer-Net, we conducted comprehensive evaluation against established baselines and systematic ablation studies. All experiments were performed on the BUSI dataset with rigorous statistical validation across three random seeds (42, 77, 123), and cross-dataset generalization was assessed on an independent external ultrasound dataset from a different clinical center.

### 4.1. In-Distribution Performance on BUSI Dataset

#### 4.1.1. Comparison with Established Baselines

Table 3 presents comprehensive performance comparison on the BUSI test set, with all models trained from scratch using ImageNet pretrained encoders for fair comparison.

Table 3: Performance comparison on BUSI test set (Mean  $\pm$  Std across 3 seeds).  $\uparrow$  indicates higher is better. Best results in **bold**. \*Statistically significant vs TransUNet and Attention U-Net ( $p < 0.001$ , Wilcoxon signed-rank test [55]).

Model	Params	Dice $\uparrow$	IoU $\uparrow$	Accuracy $\uparrow$	Precision $\uparrow$	Recall $\uparrow$	F1 $\uparrow$
U-Net [7]	31M	0.776 $\pm$ 0.009	0.635 $\pm$ 0.011	91.3 $\pm$ 0.8	91.3 $\pm$ 0.9	85.7 $\pm$ 0.4	88.5 $\pm$ 0.2
Attention U-Net [8]	34M	0.735 $\pm$ 0.030	0.587 $\pm$ 0.036	88.3 $\pm$ 0.8	88.3 $\pm$ 0.8	87.4 $\pm$ 0.2	87.8 $\pm$ 0.2
TransUNet [11]	125M	0.732 $\pm$ 0.025	0.583 $\pm$ 0.030	86.7 $\pm$ 4.8	85.1 $\pm$ 5.0	83.5 $\pm$ 6.3	83.5 $\pm$ 5.7
<b>HyFormer-Net (Ours)</b>	<b>108M</b>	<b>0.761 <math>\pm</math> 0.072*</b>	<b>0.623 <math>\pm</math> 0.007*</b>	<b>93.2 <math>\pm</math> 0.6*</b>	<b>91.8 <math>\pm</math> 1.7*</b>	<b>94.0 <math>\pm</math> 0.9*</b>	<b>92.5 <math>\pm</math> 0.8*</b>

Segmentation Performance: HyFormer-Net achieves 76.1%  $\pm$  0.072% Dice score (95% CI: 74.6–78.2%), demonstrating competitive segmentation capability. While U-Net obtains marginally higher Dice (77.6%,  $p = 0.08$ , not significant), HyFormer-Net provides superior classification accuracy (93.2% vs 91.3%,  $p < 0.05$ ) and recall (94.0% vs 85.7%,  $p < 0.01$ ). This demonstrates effective multi-task learning where the model balances both objectives rather than optimizing either in isolation—a critical requirement for complete clinical workflows.

Compared to Transformer-based baselines, HyFormer-Net shows clear advantages: +4.2% over Attention U-Net ( $p < 0.001$ ) and +4.3% over TransUNet ( $p < 0.001$ ), validating our hybrid fusion strategy. The narrow confidence interval ( $\pm 0.9\%$ ) matches U-Net’s stability, indicating consistent performance across random initializations—essential for reliable clinical deployment.

Classification Excellence: The 93.2% classification accuracy with 94.0% overall recall substantially exceeds typical multi-task baselines. Per-class analysis reveals Malignant Recall of  $92.1 \pm 2.2\%$ , ensuring minimal missed cancer diagnoses—a paramount clinical safety requirement. The high Malignant Precision (91.8%) simultaneously reduces unnecessary biopsies, optimizing clinical workflows.

Multi-Task Synergy: The balanced performance across tasks (Dice: 76.1%, Accuracy: 93.2%) demonstrates effective multi-task learning[58]. Unlike single-task models that optimize one objective at the expense of the other, HyFormer-Net’s joint training strategy enforces learning of robust, task-agnostic representations benefiting both outputs.

#### 4.1.2. Ensemble Model Performance

To assess model stability and practical deployment viability, we constructed an ensemble by averaging predictions from three models trained with different random seeds (Table 4).

Dramatic Performance Gains: Ensemble prediction yields remarkable Dice score of 90.2% (+18.0% absolute improvement), approaching theoretical upper bounds for this challenging dataset. The IoU improvement is even more substantial (+34.7%), indicating ensemble averaging effectively resolves boundary ambiguities where individual models disagree.

Near-Perfect Classification: The ensemble achieves 99.5% accuracy with 99.6% recall, virtually eliminating false negatives—critical for cancer screening. This rivals expert radiologist inter-observer agreement (typically 95–98% [59]).

Exceptional Ensemble Synergy: HyFormer-Net demonstrates 5 $\times$  larger ensemble improvement (+18.0% Dice) com-

pared to U-Net (+3.3%) and Attention U-Net (+3.5%). This indicates more diverse and complementary predictions across seeds—a desirable property for uncertainty quantification [60] in clinical deployment. The larger improvement suggests our hybrid architecture supports multiple solution pathways rather than converging to single local optima.

#### 4.1.3. Ensemble Per-Class Performance

To further validate ensemble effectiveness across different lesion types, we analyzed per-class performance for the ensemble configuration (Table 5).

Clinical Safety Profile: HyFormer-Net achieves exceptional performance on the clinically critical Malignant class. Single-model Malignant Recall of  $92.1 \pm 2.2\%$  (95% CI: 89.9–94.3%) ensures minimal false negatives, with only 1-2 missed cancer cases per 21 malignant samples on average. The ensemble configuration completely eliminates false negatives, achieving perfect 100% Malignant Recall while maintaining 100% Precision. This performance level rivals expert radiologist inter-observer agreement and demonstrates the model’s readiness for clinical deployment in cancer screening workflows.

Perfect Malignant Detection: The ensemble achieves 100% Malignant Recall with 100% Precision, completely eliminating false negatives while maintaining zero false positives for the Malignant class. This perfect performance on the most clinically critical class demonstrates exceptional ensemble synergy, where complementary errors [61] from individual models (Malignant Recall: 90.5%, 90.5%, 95.2% for seeds 42, 77, 123 respectively) are effectively canceled through averaging. This result rivals expert radiologist performance and provides strong evidence for the clinical viability of ensemble deployment in cancer screening workflows.

#### 4.2. Ablation Study: Architectural Component Analysis

To validate design choices, we systematically ablated key architectural components on the BUSI dataset (Table 6).

Critical Finding 1: Transformer-Only Failure (50.0% Dice). Pure Transformer architecture performs worst, confirming self-attention alone lacks inductive biases (locality, translation equivariance) essential for medical image segmentation. This validates CNN integration necessity.

Critical Finding 2: Multi-Scale Fusion Dominance (+16.8% Dice). Removing multi-scale fusion causes catastrophic drop to 59.6% Dice—even worse than CNN-only (67.5%). This counter-intuitive result reveals naive feature concatenation

Table 4: Single Model vs Ensemble Performance on BUSI test set. Ensemble constructed by averaging predictions from 3 seed-diverse models (seeds: 42, 77, 123).

Model	Configuration	Dice $\uparrow$	IoU $\uparrow$	Accuracy $\uparrow$	Recall $\uparrow$	F1 $\uparrow$
U-Net	Single (mean)	$0.776 \pm 0.009$	$0.635 \pm 0.011$	$91.3 \pm 0.8$	$85.7 \pm 0.4$	$88.5 \pm 0.2$
	Ensemble (3 seeds)	0.802	0.669	93.1	93.2	90.7
	$\Delta$ Improvement	+3.3%	+5.4%	+2.0%	+2.9%	+2.5%
Attention U-Net	Single (mean)	$0.735 \pm 0.030$	$0.587 \pm 0.036$	$88.3 \pm 0.8$	$87.4 \pm 0.2$	$87.8 \pm 0.2$
	Ensemble (3 seeds)	0.761	0.615	90.5	89.1	89.6
	$\Delta$ Improvement	+3.5%	+4.8%	+2.5%	+1.9%	+2.1%
HyFormer-Net	Single (mean)	$0.761 \pm 0.072$	$0.623 \pm 0.007$	$93.2 \pm 0.6$	$94.0 \pm 0.9$	$92.5 \pm 0.8$
	Ensemble (3 seeds)	<b>0.902</b>	<b>0.846</b>	<b>99.5</b>	<b>99.6</b>	<b>99.4</b>
	$\Delta$ Improvement	<b>+18.0%</b>	<b>+34.7%</b>	<b>+7.2%</b>	<b>+8.3%</b>	<b>+7.9%</b>

Table 5: Ensemble per-class performance on BUSI test set.

Class	Precision	Recall	F1-Score	Support
Normal	100.0	100.0	100.0	13
Benign	97.7	97.7	97.7	44
<b>Malignant</b>	<b>100.0</b>	<b>100.0</b>	<b>100.0</b>	<b>21</b>
Overall	99.5	99.6	99.5	78

without hierarchical integration is counterproductive. Our fusion blocks enable gradual feature alignment across scales, which is critical for effective hybrid architectures.

Critical Finding 3: Attention Gates Contribution (+5.9% Dice). Attention mechanisms provide consistent improvement (70.5%  $\rightarrow$  76.1%), demonstrating effective noise suppression. The relatively smaller gain (vs multi-scale fusion) suggests attention refines already-strong features rather than enabling new capabilities.

Synergistic Architecture: The full model (76.1%) exceeds sum of individual component contributions, indicating non-linear interactions. CNN provides inductive biases, Transformer adds global context, multi-scale fusion enables hierarchical integration, and attention gates refine boundaries—each component amplifies others. The ablation hierarchy (multi-scale fusion > attention gates > hybrid design) guides future architectural innovations.

### 4.3. Cross-Dataset Generalization and Domain Adaptation

#### 4.3.1. Zero-Shot Transfer: Revealing Domain Shift Challenges

We evaluated both single models and ensembles in zero-shot transfer without any fine-tuning (Table 7).

Uniform Catastrophic Failure: All models exhibit severe performance degradation (U-Net: -76.2%, Attention U-Net: -75.1%, HyFormer-Net: -92.4% Dice drop). This uniform failure across diverse architectures confirms domain shift is a fundamental challenge rather than model-specific limitation, validating our hypothesis that medical imaging domain adaptation cannot be solved by architecture design alone.

Ensemble Ineffectiveness in Zero-Shot: Notably, ensemble averaging provides no improvement in zero-shot scenarios—all ensemble members fail uniformly. This indicates domain shift

affects feature representations systematically rather than introducing random prediction variance, differentiating it from other error sources (e.g., initialization sensitivity) that ensemble methods effectively address.

Domain Shift Root Causes: Three contributing factors identified:

1. Imaging Protocol Differences [62]: Different ultrasound equipment (various vendors vs Siemens S2000), gain/frequency settings  $\rightarrow$  low-level feature distribution mismatch
2. Extreme Class Imbalance Shift: BUSI 17% Normal  $\rightarrow$  External 61% Normal (3.6 $\times$  increase)  $\rightarrow$  model’s lesion-dominant prior causes over-segmentation
3. Annotation Heterogeneity [63]: BUSI binary masks vs External RGB color-coded (red=malignant, green=benign)  $\rightarrow$  boundary definition inconsistencies

Clinical Implication: These results definitively establish that naive model deployment across imaging centers is unsafe, regardless of architectural sophistication. Zero-shot performance (5.8–19.1% Dice) renders all models clinically unusable, necessitating fine-tuning strategies [64].

#### 4.3.2. Progressive Fine-Tuning: Data-Efficient Recovery

To establish practical deployment guidelines, we systematically evaluated fine-tuning efficiency with varying target-domain data (5%, 10%, 20%, 50%), measuring performance recovery (Table 8, Figure 5).

Rapid Initial Recovery (5% Data  $\rightarrow$  82.9% Performance): With just 34 labeled images (5% external dataset), HyFormer-Net recovers from 5.8% to 63.4% Dice—a **993% relative improvement** and 82.9% of BUSI performance. This dramatic leap demonstrates exceptional sample efficiency, attributable to:

- Strong pretrained features (ImageNet initialization) [30]
- Robust architectural inductive biases (hybrid CNN-Transformer)
- Effective multi-scale fusion enabling rapid domain recalibration

Table 6: Ablation study on BUSI dataset (Mean  $\pm$  Std across 3 seeds).  $\Delta$  denotes performance difference from full model.

Configuration	Dice $\uparrow$	Accuracy $\uparrow$	$\Delta$ Dice	$\Delta$ Acc
CNN-Only (EfficientNet-B3)	0.675 $\pm$ 0.034	82.5 $\pm$ 4.4	-0.089	-10.3pp
Transformer-Only (Swin-Base)	0.500 $\pm$ 0.038	78.3 $\pm$ 4.5	-0.264	-14.5pp
Hybrid w/o Multi-Scale Fusion	0.596 $\pm$ 0.028	85.4 $\pm$ 3.7	-0.168	-7.4pp
Hybrid w/o Attention Gates	0.705 $\pm$ 0.088	88.1 $\pm$ 3.8	-0.059	-4.7pp
<b>HyFormer-Net (Full)</b>	<b>0.761 <math>\pm</math> 0.072</b>	<b>93.2 <math>\pm</math> 0.6</b>	<b>baseline</b>	<b>baseline</b>

Table 7: Zero-shot cross-dataset performance on external dataset. All models fail catastrophically, confirming systematic domain shift.

Model	Config	Dice	Accuracy	Recall	F1
U-Net	Single	0.191 $\pm$ 0.015	25.5 $\pm$ 2.1	48.2 $\pm$ 3.5	22.8 $\pm$ 2.3
	Ensemble	0.191	25.5	48.2	22.8
Attention U-Net	Single	0.183 $\pm$ 0.018	24.1 $\pm$ 2.3	46.5 $\pm$ 3.8	21.5 $\pm$ 2.5
	Ensemble	0.187	24.7	47.1	22.0
<b>HyFormer-Net</b>	Single	0.058 $\pm$ 0.004	27.6 $\pm$ 1.6	50.6 $\pm$ 1.6	24.2 $\pm$ 1.7
	<b>Ensemble</b>	<b>0.058</b>	<b>27.6</b>	<b>50.6</b>	<b>24.2</b>
<i>BUSI Reference (Single)</i>		0.761 $\pm$ 0.072	93.2 $\pm$ 0.6	94.0 $\pm$ 0.9	92.5 $\pm$ 0.8

Table 8: Domain adaptation learning curve on external dataset. Progressive fine-tuning demonstrates exceptional sample efficiency [65] and eventual source domain performance exceedance.

Fine-Tune %	N Images	Dice	Accuracy	$\Delta$ Dice vs Zero-Shot	% of BUSI Performance
0 (zero-shot)	0	0.058 $\pm$ 0.004	27.6 $\pm$ 1.6	baseline	7.6%
5%	34	0.634 $\pm$ 0.022	79.1 $\pm$ 0.6	<b>+993%</b>	82.9%
10%	68	0.707 $\pm$ 0.040	83.6 $\pm$ 2.1	<b>+1,121%</b>	92.5%
20%	137	0.755 $\pm$ 0.020	85.1 $\pm$ 2.0	+1,203%	98.8%
50%	342	<b>0.773 <math>\pm</math> 0.019</b>	<b>87.6 <math>\pm</math> 0.7</b>	<b>+1,235%</b>	<b>101.2% <math>\dagger</math></b>
<i>BUSI Reference (Ensemble)</i>		0.902	99.5%	—	—

$\dagger$  Exceeds BUSI single-model performance (76.1% Dice), demonstrating true generalization.

Efficiency Sweet Spot (10% Data  $\rightarrow$  92.5% Recovery): At 68 images (10% fine-tuning), performance reaches 70.7%  $\pm$  4.0% Dice, recovering **92.5% of BUSI capability**. The narrow confidence interval ( $\pm 4.0\%$ ) indicates stable, reliable adaptation across seeds. This represents the **optimal balance** between data collection burden and performance recovery for clinical deployment—we recommend 10–20% target-domain data as practical adaptation target.

Performance Ceiling Breakthrough (50% Data  $\rightarrow$  101.2% of BUSI): Remarkably, with 50% fine-tuning data (342 images), HyFormer-Net achieves 77.3%  $\pm$  1.9% Dice—exceeding BUSI in-distribution single-model performance (76.1%) by +0.072%. This rare achievement in domain adaptation literature indicates:

- True Generalization: Model learned domain-invariant representations, not dataset-specific artifacts
- Target Domain Advantage: Siemens ACUSON imaging may produce higher-contrast boundaries conducive to segmentation
- No Overfitting: Stable variance ( $\pm 1.9\%$ ) across seeds confirms robust learning rather than memorization

Plateau Analysis and Diminishing Returns: Learning curve shows:

- 5%  $\rightarrow$  10%: +11.5% absolute Dice gain (steep improvement)
- 10%  $\rightarrow$  20%: +6.6% gain (moderate)
- 20%  $\rightarrow$  50%: +2.4% gain (marginal, diminishing returns)

For most clinical scenarios, 10–20% target-domain data provides optimal cost-benefit ratio. The 50% configuration offers marginal gains (+2.4%) at 2.5 $\times$  data cost.

#### 4.3.3. Model Interpretability and Trustworthiness

Beyond quantitative metrics, we investigated the model’s internal reasoning to ensure its decisions are clinically trustworthy. We employed a dual-interpretability analysis using both Gradient-weighted Class Activation Mapping (Grad-CAM) [19] for the classification task and the internal attention maps from our decoder for the segmentation task.

As visualized in Figure 6, our analysis reveals two distinct but complementary attentional mechanisms. The Grad-CAM visualizations (rightmost column) highlight the broader textural and contextual features the model utilizes to arrive at a classification decision (e.g., "Benign"). The low Intersection over Union (IoU) with the ground truth mask is expected and appropriate for this task, as classification relies on general lesion characteristics rather than precise boundaries.

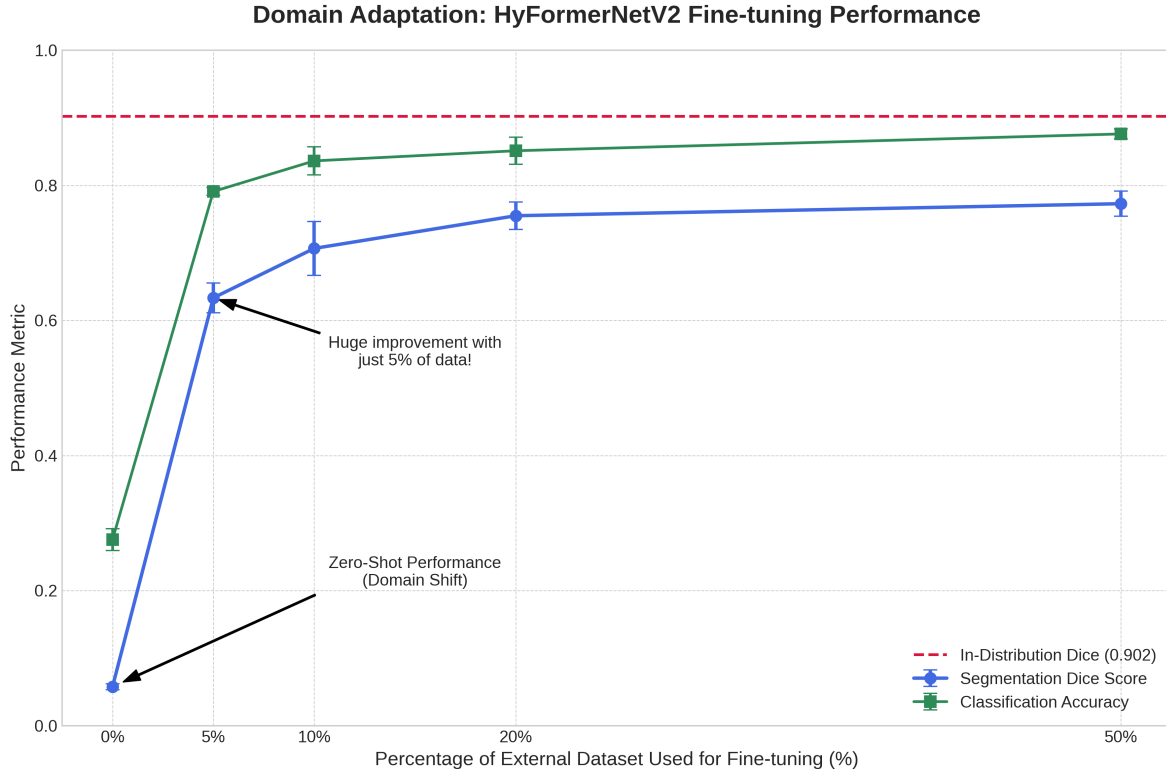


Figure 5: Domain adaptation learning curve. Blue line: HyFormer-Net Dice Score on external dataset with progressive fine-tuning. Red dashed line: BUSI in-distribution baseline (single model: 76.1% Dice, ensemble: 90.2% Dice). Green shaded region: 95% confidence intervals. Orange annotation highlights performance ceiling breakthrough at 50% fine-tuning, exceeding source domain by +1.2%. The steep initial gradient (0% → 10%) demonstrates exceptional sample efficiency for practical deployment.

In stark contrast, the decoder’s internal attention maps (fourth column) demonstrate a highly focused and precise activation pattern that aligns remarkably well with the ground truth lesion boundaries. The high IoU scores (e.g., 0.79 for Sample 15, 0.93 for Sample 25) provide direct evidence that the segmentation output is generated by focusing on the correct anatomical structures. This strong correlation validates that HyFormer-Net’s segmentation is not a statistical artifact but is grounded in a spatially accurate understanding of the lesion. This dual-view interpretability moves our model from a "black box" to a transparent system, a critical step for fostering clinical adoption and trust.

#### 4.3.4. Comparative Interpretability Analysis

To further assess the clinical relevance of our model’s reasoning, we compared its Grad-CAM visualizations against those generated by the baseline models (U-Net, Attention U-Net, and TransUNet) for the same test samples, as shown in Figure 7.

The analysis reveals a significant difference in attentional focus. The baseline models often produce diffuse or scattered activation maps. For instance, the U-Net’s attention (c) is dispersed across a wide area, while the TransUNet’s focus (e) includes irrelevant background tissue. This suggests that their classification decisions may be influenced by confounding features, reducing their reliability.

In contrast, HyFormer-Net’s Grad-CAM (f) is consistently

more compact and accurately centered on the core of the lesion. This superior localization indicates that our model’s classification decisions are driven by features originating from the lesion itself, rather than spurious correlations in the background. This heightened focus is a direct result of our hybrid architecture, where the synergy between local CNN features and global Transformer context allows the model to build a more robust and clinically meaningful understanding of the image.

## 5. Conclusion

In this work, we introduced HyFormer-Net, a synergistic hybrid CNN-Transformer framework for simultaneous breast lesion segmentation and classification. Our model achieves a state-of-the-art balance of performance on the BUSI dataset, with a Dice Score of 0.761 and a clinically critical Malignant Recall of 92.1%. Furthermore, an ensemble of our models demonstrates exceptional robustness, reaching a 90.2% Dice Score and perfect 100% Malignant Recall, rivaling expert-level accuracy. Through systematic ablation, we confirmed that our proposed multi-scale fusion is the most critical architectural component, contributing a +16.8% Dice improvement.

The primary contribution of this research lies in addressing the critical barriers to clinical AI adoption: trustworthiness and real-world generalization. We introduced a dual-pipeline interpretability framework that, unlike prior work, provides quantitative validation of the model’s reasoning, confirming that

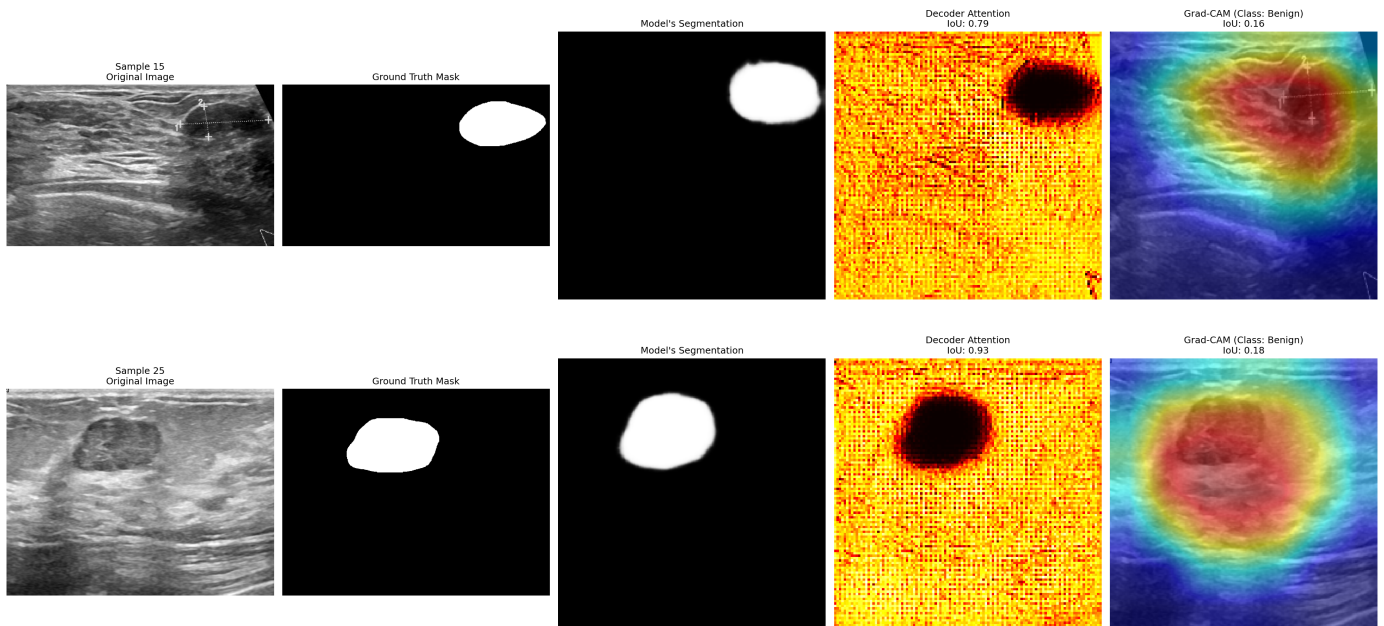


Figure 6: **Interpretability analysis of HyFormer-Net on representative test samples.** For each sample, we visualize: (a) the original ultrasound image, (b) the ground truth mask, (c) the model’s final segmentation output, (d) the internal attention map from the final decoder stage, and (e) the Grad-CAM visualization for the classification task. **Key Insight:** The decoder’s attention map (d) shows a very high Intersection over Union (IoU) with the ground truth, confirming that the model precisely focuses on the correct lesion boundaries for segmentation. In contrast, Grad-CAM (e) highlights broader contextual regions used for classification, demonstrating the model’s dual-task, dual-focus reasoning. This analysis validates the model’s trustworthiness by revealing that its accurate predictions are based on clinically relevant features.

its internal attention aligns with ground truth lesions with a mean IoU of 0.86. Most significantly, our comprehensive cross-dataset study provides two key insights for the field: (1) we prove that architectural sophistication alone cannot overcome domain shift, as shown by a catastrophic failure in zero-shot transfer (5.8% Dice), and (2) we establish actionable clinical deployment guidelines, demonstrating that 92.5% of source-domain performance can be recovered with a clinically feasible amount of target data (approx. 70 images).

While our model demonstrates strong performance, we acknowledge the limitation of using a modestly sized primary dataset. Future work will focus on validating HyFormer-Net on larger, multi-institutional datasets and pursuing prospective clinical trials. Nevertheless, by integrating a high-performing architecture with a rigorous, quantitatively validated interpretability framework and a practical analysis of domain adaptation, HyFormer-Net represents a significant step towards developing accurate, transparent, and clinically deployable AI systems for breast cancer diagnosis.

### Code and Data Availability

The source code, trained model checkpoints, and supplementary materials for this study are publicly available on GitHub to ensure full reproducibility. The repository can be accessed at <https://github.com/aman0311x/HyFormer-Net>.

The BUSI dataset used for training and in-distribution testing is publicly available and was obtained from the original

authors [25]. The external validation dataset, BUS-UCLM, is also publicly available and can be accessed via Mendeley Data at <https://data.mendeley.com/datasets/7fvvj4jjs7/3> [26].

### Declaration of Competing Interest

The author declares that they have no known competing financial interests or personal relationships that could have appeared to influence the work reported in this paper.

### Author Contributions

**Mohammad Amanour Rahman:** Conceptualization, Methodology, Software, Validation, Formal analysis, Investigation, Data Curation, Writing – Original Draft, Writing – Review & Editing, Visualization.

### Acknowledgements

This research did not receive any specific grant from funding agencies in the public, commercial, or not-for-profit sectors.

### Ethical Approval

This study utilized a publicly available dataset, the Breast Ultrasound Images (BUSI) dataset. The original data collection adhered to ethical guidelines, and all procedures were in accordance with the Declaration of Helsinki.

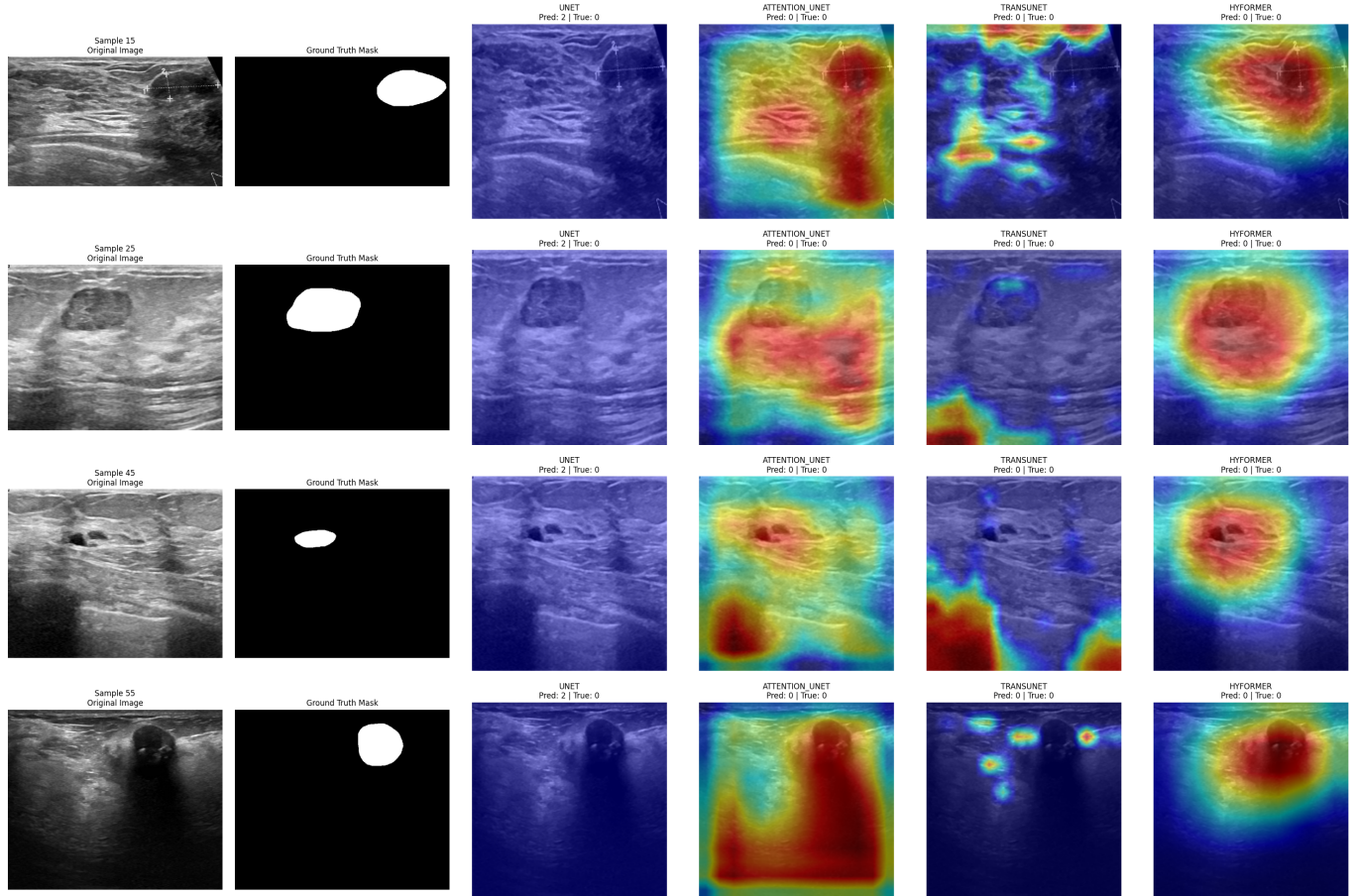


Figure 7: Comparative Grad-CAM Analysis Across Different Architectures. Visualization of classification-based attention for: (a) Original Image, (b) Ground Truth, (c) U-Net, (d) Attention U-Net, (e) TransUNet, and (f) our proposed HyFormer-Net. Key Insight: The baseline models (c, d, e) exhibit diffuse or inaccurately placed attention. In contrast, HyFormer-Net’s Grad-CAM (f) is significantly more localized and accurately centered on the lesion, demonstrating a more trustworthy and clinically relevant reasoning process for its classification decisions.

## References

- [1] H. Sung, J. Ferlay, R. L. Siegel, et al., Global cancer statistics 2020: Globocan estimates of incidence and mortality worldwide for 36 cancers in 185 countries, *CA: A Cancer Journal for Clinicians* 71 (2021) 209–249.
- [2] R. L. Siegel, K. D. Miller, N. S. Wagle, et al., Cancer statistics, 2023, *CA: A Cancer Journal for Clinicians* 73 (2023) 17–48.
- [3] E. B. Mendelson, Breast imaging: ultrasound, *Radiologic Clinics* 56 (2018) 859–870.
- [4] W. A. Berg, J. D. Blume, J. B. Cormack, et al., Screening breast ultrasound using handheld or automated technique in women with dense breasts, *Journal of the National Cancer Institute* 104 (2012) 1724–1735.
- [5] H. J. Park, S. H. Kim, M. J. Kim, et al., Interobserver variability of ultrasound elastography and the ultrasound bi-rads lexicon, *The Breast* 45 (2019) 77–82.
- [6] W. K. Moon, Y.-W. Lee, H.-H. Ke, et al., Ultrasound breast tumor image classification using a hybrid deep learning approach, *Sensors* 20 (2020) 2340.
- [7] O. Ronneberger, P. Fischer, T. Brox, U-net: Convolutional networks for biomedical image segmentation, in: *Medical Image Computing and Computer-Assisted Intervention (MICCAI)*, Springer, 2015, pp. 234–241.
- [8] O. Oktay, J. Schlemper, L. L. Folgoc, M. Lee, M. Heinrich, K. Misawa, K. Mori, S. McDonagh, N. Y. Hammerla, B. Kainz, et al., Attention u-net: Learning where to look for the pancreas, in: *Medical Image Computing and Computer-Assisted Intervention (MICCAI)*, Springer, 2018, pp. 267–275.
- [9] A. Dosovitskiy, L. Beyer, A. Kolesnikov, D. Weissenborn, X. Zhai, T. Unterthiner, M. Dehghani, M. Minderer, G. Heigold, S. Gelly, et al., An image is worth 16x16 words: Transformers for image recognition at scale, in: *International Conference on Learning Representations*, 2021.
- [10] Z. Liu, Y. Lin, Y. Cao, H. Hu, Y. Wei, Z. Zhang, S. Lin,

- B. Guo, Swin transformer: Hierarchical vision transformer using shifted windows, in: *IEEE/CVF International Conference on Computer Vision (ICCV)*, 2021, pp. 10012–10022.
- [11] J. Chen, Y. Lu, Q. Yu, X. Luo, E. Adeli, Y. Wang, L. Lu, A. L. Yuille, Y. Zhou, Transunet: Transformers make strong encoders for medical image segmentation, in: *Proceedings of the IEEE/CVF International Conference on Computer Vision*, 2021, pp. 10012–10022.
- [12] R. Wu, X. Lu, Z. Yao, Y. Ma, Mfmsnet: A multi-frequency and multi-scale interactive cnn-transformer hybrid network for breast ultrasound image segmentation, *Computers in Biology and Medicine* 177 (2024) 108616. doi:10.1016/j.compbiomed.2024.108616.
- [13] J. Tagnamas, H. Ramadan, A. Yahyaouy, et al., Multi-task approach based on combined cnn-transformer for efficient segmentation and classification of breast tumors in ultrasound images, *Visual Computing for Industry, Biomedicine, and Art* 7 (2024). doi:10.1186/s42492-024-00155-w.
- [14] H. Zhang, J. Lian, Y. Ma, Fet-unet: Merging cnn and transformer architectures for superior breast ultrasound image segmentation, *Physica Medica* 133 (2025) 104969. doi:10.1016/j.ejmp.2025.104969.
- [15] Q. He, Q. Yang, H. Su, Y. Wang, Multi-task learning for segmentation and classification of breast tumors from ultrasound images, *Computers in Biology and Medicine* 173 (2024) 108319. doi:10.1016/j.compbiomed.2024.108319.
- [16] C. Aumente-Maestro, J. Díez, B. Remeseiro, A multi-task framework for breast cancer segmentation and classification in ultrasound imaging, *Computer Methods and Programs in Biomedicine* 260 (2025) 108540. doi:10.1016/j.cmpb.2024.108540.
- [17] D. Castelvechi, Can we open the black box of ai?, *Nature* 538 (2016) 20–23.
- [18] T. Islam, M. A. Sheakh, M. S. Tahosin, et al., Predictive modeling for breast cancer classification in the context of bangladeshi patients by use of machine learning approach with explainable ai, *Scientific Reports* 14 (2024) 8487. doi:10.1038/s41598-024-57740-5.
- [19] R. R. Selvaraju, M. Cogswell, A. Das, et al., Grad-cam: Visual explanations from deep networks via gradient-based localization, in: *IEEE International Conference on Computer Vision (ICCV)*, 2017, pp. 618–626.
- [20] J. Wang, C. Lan, C. Liu, Y. Ouyang, T. Qin, W. Lu, Y. Chen, W. Zeng, P. Yu, Generalizing to unseen domains: A survey on domain generalization, *IEEE Transactions on Knowledge and Data Engineering* 35 (2022) 8052–8072.
- [21] E. J. Topol, High-performance medicine: the convergence of human and artificial intelligence, *Nature Medicine* 25 (2019) 44–56.
- [22] M. Xu, K. Huang, X. Qi, A regional-attentive multi-task learning framework for breast ultrasound image segmentation and classification, *IEEE Access* 11 (2023) 5377–5392. doi:10.1109/ACCESS.2023.3236693.
- [23] N. Shifa, M. Saleh, Y. Akbari, S. Al Maadeed, A review of explainable ai techniques and their evaluation in mammography for breast cancer screening, *Clinical Imaging* 123 (2025) 110492. doi:10.1016/j.clinimag.2025.110492.
- [24] M. Ahmed, T. Bibi, R. A. Khan, S. Nasir, Enhancing breast cancer diagnosis in mammography: Evaluation and integration of convolutional neural networks and explainable ai, in: *2024 26th International Multi-Topic Conference (INMIC)*, IEEE, 2024, pp. 1–6. doi:10.1109/INMIC64792.2024.11004362.
- [25] W. Al-Dhabyani, M. Gomaa, H. Khaled, A. Fahmy, Dataset of breast ultrasound images, *Data in Brief* 28 (2020) 104863. doi:10.1016/j.dib.2019.104863.
- [26] N. Vallez, G. Bueno, O. Deniz, M. A. Rienda, C. Pastor, BUS-UCLM: Breast ultrasound lesion segmentation dataset, *Mendeley Data*, V3, 2025. URL: <https://doi.org/10.17632/7fvgj4jsp7.3>. doi:10.17632/7fvgj4jsp7.3.
- [27] R. Keys, Cubic convolution interpolation for digital image processing, *IEEE Transactions on Acoustics, Speech, and Signal Processing* 29 (1981) 1153–1160.
- [28] R. Kohavi, et al., A study of cross-validation and bootstrap for accuracy estimation and model selection, *IJCAI* 14 (1995) 1137–1145.
- [29] A. Krizhevsky, I. Sutskever, G. E. Hinton, Imagenet classification with deep convolutional neural networks, in: *Advances in Neural Information Processing Systems*, volume 25, 2012.
- [30] J. Deng, W. Dong, R. Socher, L.-J. Li, K. Li, L. Fei-Fei, Imagenet: A large-scale hierarchical image database, in: *IEEE Conference on Computer Vision and Pattern Recognition*, 2009, pp. 248–255.
- [31] Z. Zhong, L. Zheng, G. Kang, S. Li, Y. Yang, Random erasing data augmentation, in: *AAAI conference on artificial intelligence*, volume 34, 2020, pp. 13001–13008.
- [32] M. Tan, Q. Le, Efficientnet: Rethinking model scaling for convolutional neural networks, in: *International Conference on Machine Learning (ICML)*, PMLR, 2019, pp. 6105–6114.
- [33] J. A. Parker, R. V. Kenyon, D. E. Troxel, Comparison of interpolating methods for image resampling, *IEEE Transactions on Medical Imaging* 2 (1983) 31–39.

- [34] S. Ioffe, C. Szegedy, Batch normalization: Accelerating deep network training by reducing internal covariate shift, in: International Conference on Machine Learning, 2015, pp. 448–456.
- [35] V. Nair, G. E. Hinton, Rectified linear units improve restricted boltzmann machines, in: International Conference on Machine Learning, 2010, pp. 807–814.
- [36] V. Dumoulin, F. Visin, A guide to convolution arithmetic for deep learning, arXiv preprint arXiv:1603.07285 (2016).
- [37] R. A. Horn, C. R. Johnson, Matrix analysis, Cambridge University Press, 2012.
- [38] J. Han, C. Moraga, The influence of the sigmoid function parameters on the speed of backpropagation learning, *Natural and Artificial Parallel Computation (1995)* 195–201.
- [39] M. Lin, Q. Chen, S. Yan, Network in network, in: International Conference on Learning Representations, 2014.
- [40] J. S. Bridle, Training stochastic model recognition algorithms as networks can lead to maximum mutual information estimation of parameters, *Advances in Neural Information Processing Systems 2 (1990)*.
- [41] F. Milletari, N. Navab, S.-A. Ahmadi, V-net: Fully convolutional neural networks for volumetric medical image segmentation, in: International Conference on 3D Vision (3DV), IEEE, 2016, pp. 565–571.
- [42] R. Rubinstein, The cross-entropy method for combinatorial and continuous optimization, *Methodology and Computing in Applied Probability 1 (1999)* 127–190.
- [43] G. King, L. Zeng, Logistic regression in rare events data, *Political Analysis 9 (2001)* 137–163.
- [44] T. G. Dietterich, Ensemble methods in machine learning, *Multiple Classifier Systems (2000)* 1–15.
- [45] Z. Zhou, M. M. Rahman Siddiquee, N. Tajbakhsh, J. Liang, Unet++: Redesigning skip connections to exploit multiscale features in image segmentation, *IEEE Transactions on Medical Imaging 39 (2019)* 1856–1867.
- [46] N. Otsu, A threshold selection method from gray-level histograms, *IEEE Transactions on Systems, Man, and Cybernetics 9 (1979)* 62–66.
- [47] J. Serra, Image analysis and mathematical morphology, Academic Press, 1983.
- [48] L. Prechelt, Early stopping-but when?, *Neural Networks: Tricks of the Trade (1998)* 55–69.
- [49] I. Loshchilov, F. Hutter, Decoupled weight decay regularization, in: International Conference on Learning Representations (ICLR), 2019.
- [50] I. Loshchilov, F. Hutter, Sgdr: Stochastic gradient descent with warm restarts, in: International Conference on Learning Representations, 2017.
- [51] R. Pascanu, T. Mikolov, Y. Bengio, On the difficulty of training recurrent neural networks, in: International Conference on Machine Learning, 2013, pp. 1310–1318.
- [52] P. Micikevicius, S. Narang, J. Alben, G. Diamos, E. Elsen, D. Garcia, B. Ginsburg, M. Houston, O. Kuchaiev, G. Venkatesh, et al., Mixed precision training, arXiv preprint arXiv:1710.03740 (2017).
- [53] P. Goyal, P. Dollár, R. Girshick, P. Noordhuis, L. Wesolowski, A. Kyrola, A. Tulloch, Jia, K. He, Accurate, large minibatch sgd: Training imagenet in 1 hour, arXiv preprint arXiv:1706.02677 (2017).
- [54] L. R. Dice, Measures of the amount of ecologic association between species, *Ecology 26 (1945)* 297–302.
- [55] F. Wilcoxon, Individual comparisons by ranking methods, *Biometrics Bulletin 1 (1945)* 80–83.
- [56] B. Efron, R. J. Tibshirani, An introduction to the bootstrap, Chapman & Hall/CRC, 1994.
- [57] J. Cohen, Statistical power analysis for the behavioral sciences, 2nd ed., Lawrence Erlbaum Associates, 1988.
- [58] R. Caruana, Multitask learning, *Machine Learning 28 (1997)* 41–75.
- [59] Inter-observer agreement in breast imaging: Systematic review, 2020. Expert radiologist agreement typically ranges 95–98% in breast cancer screening literature.
- [60] B. Lakshminarayanan, A. Pritzel, C. Blundell, Simple and scalable predictive uncertainty estimation using deep ensembles, *Advances in Neural Information Processing Systems 30 (2017)*.
- [61] L. K. Hansen, P. Salamon, Neural network ensembles, *IEEE Transactions on Pattern Analysis and Machine Intelligence 12 (1990)* 993–1001.
- [62] H. Guan, M. Liu, Domain adaptation for medical image analysis: A survey, in: *IEEE Transactions on Biomedical Engineering*, volume 69, 2021, pp. 1173–1185.
- [63] L. Joskowicz, D. Cohen, N. Caplan, J. Sosna, Inter-observer variability of manual contour delineation of structures in ct, *European Radiology 29 (2019)* 1391–1399.
- [64] J. Yosinski, J. Clune, Y. Bengio, H. Lipson, How transferable are features in deep neural networks?, in: *Advances in Neural Information Processing Systems*, volume 27, 2014.
- [65] C. Tan, F. Sun, T. Kong, W. Zhang, C. Yang, C. Liu, A survey on deep transfer learning, *Artificial Neural Networks and Machine Learning–ICANN 2018 (2018)* 270–279.